



*Citation for published version:*

Zhang, M, Zhu, L, Wang, H, Li, Y, Soleimani, M & Yang, Y 2021, 'Multiple Measurement Vector Based Complex-Valued Multi-Frequency ECT', *IEEE Transactions on Instrumentation and Measurement*, vol. 70, 9298884. <https://doi.org/10.1109/TIM.2020.3045842>

*DOI:*

[10.1109/TIM.2020.3045842](https://doi.org/10.1109/TIM.2020.3045842)

*Publication date:*

2021

*Document Version*

Peer reviewed version

[Link to publication](#)

© 2020 IEEE. Personal use of this material is permitted. Permission from IEEE must be obtained for all other users, including reprinting/ republishing this material for advertising or promotional purposes, creating new collective works for resale or redistribution to servers or lists, or reuse of any copyrighted components of this work in other works.

**University of Bath**

## **Alternative formats**

If you require this document in an alternative format, please contact:  
[openaccess@bath.ac.uk](mailto:openaccess@bath.ac.uk)

### **General rights**

Copyright and moral rights for the publications made accessible in the public portal are retained by the authors and/or other copyright owners and it is a condition of accessing publications that users recognise and abide by the legal requirements associated with these rights.

### **Take down policy**

If you believe that this document breaches copyright please contact us providing details, and we will remove access to the work immediately and investigate your claim.

# Multiple Measurement Vector Based Complex-Valued Multi-Frequency ECT

Maomao Zhang, Member, IEEE, Liying Zhu, Haokun Wang, Yi Li, Member, IEEE, Manuchehr Soleimani, Member, IEEE, and Yunjie Yang, Member, IEEE

**Abstract**—Complex-Valued, Multi-Frequency Electrical Capacitance Tomography (CVMF-ECT) is a recently developed tomographic concept which is capable to simultaneously reconstruct spectral permittivity and conductivity properties of target objects within the region of interest. To date, this concept has been limited to simulation and another key issue restricting its wide adoption lies in its poor image quality. This paper reports a CVMF-ECT system to verify its practical feasibility and further proposes a novel image reconstruction framework to effectively and efficiently reconstruct multi-frequency images using complex-valued capacitance data. The image reconstruction framework utilizes the inherent spatial correlations of the multi-frequency images as a priori information and encodes it by using Multiple Measurement Vector (MMV) model. Alternating direction method of multipliers was introduced to solve the MMV problem. Real-world experiments validate the feasibility of CVMF-ECT, and MMV based CVMF-ECT method demonstrates superior performance compared to conventional ECT approaches.

**Index Terms**—Complex-valued measurement, electrical capacitance tomography, image reconstruction, multiple frequency, multiple measurement vector

## I. INTRODUCTION

ELECTRICAL Capacitance Tomography (ECT) is an emerging imaging technique which can reconstruct the permittivity distribution of dielectric materials within the Region of Interest (ROI) [1]. A prevailing application of ECT is multiphase flow measurement, where ECT can visualize the flow regime and derive critical flow parameters with externally deployed sensor electrodes in a real-time, non-invasive and contactless manner [2-6]. In ECT, capacitance measurements are mainly dependent on the dielectric permittivity of the Material Under Testing (MUT), and the conductive property of the MUT is normally negligible. In gas/oil/water multiphase flows, the water content over 40% is normally very challenging for conventional ECT, as the admittance obtained from an ECT measurement unit is mainly determined by the conductivity of the water, rather than the permittivity of MUT. To address this issue, Liu *et al* implemented Electrical Resistance Tomography (ERT) as a supplementary method to deal with multiphase flows with a high water content [7]. However, ERT sensors require direct contact with the conductive media, which is not

suitable for long-term metering in oil wells, since the wax or deposits might stick to the electrodes and block the conductive path between electrodes. To avoid direct contact with the flow, Hammer *et al* proposed high frequency magnetic methods for two phase flow measurement [8-10]. Another contactless tomography modality, i.e. Magnetic Induction Tomography (MIT), was introduced by Zhang *et al* [11] to guide ECT to distinguish the non-conductive samples from the background of conductive liquids. MIT is an imaging technique using coils to sense the secondary magnetic field from the eddy current inside the conductive liquid, where the conductivity of the liquid should be high enough to achieve a sensible level. To find a method to deal with a large range of conductivity, Wang *et al* proposed Capacitively Coupled Electrical Resistance Tomography (CCERT), which applied ECT sensors to collect resistance information, and reconstruct the conductivity distribution with high water contents [12-14]. In addition, Gunes *et al* proposed the concept of Displacement-Current Phase Tomography (DCPT) using the phase information from the ECT measurement to reconstruct the loss factor distribution of MUT [15, 16]. Jiang *et al* proposed a method to link the conductivity distribution with the phase difference on impedance measurements [17]. Recently, Zhang *et al* has developed a Complex-Valued, Multi-Frequency Electrical Capacitance Tomography (CVMF-ECT) model, simulated the complex-valued capacitance measurements and reconstructed both permittivity and conductivity by using measurements from a simulated 8-electrode ECT sensor [18]. Overall, these contactless methods based on either typical ECT sensors or capacitive sensor arrays aim to recover both permittivity and conductivity distribution from impedance or admittance measurements in the scenarios where conductivity is non-negligible.

In traditional ECT, applying excitation voltage with different frequencies does not provide more information of permittivity distribution. Capacitance measurement of dielectric MUT is independent of frequency, whilst MUT with conductivity could be frequency-dependent, *i.e.* change of excitation frequency can generate additional information or help distinguish the target objects from background. Especially in the case of gas/oil/water flow measurement, the salinity in the produced water could be considerable, leading to very high conductivity. To reduce the effect of increasing conductivity, the frequency of excitation signal must be increased [17-20].

To date, the study of CVMF-ECT has been mainly simulation-based, and existing image reconstruction methods for CVMF-ECT are based on Single-Measurement Vector (SMV) model [18], where the capacitance measurement obtained under each frequency is processed individually. In this paper, we report a CVMF-ECT system to assess its practical feasibility and propose a novel image reconstruction framework based on Multiple Measurement Vector (MMV) model [21]. The proposed MMV framework utilizes simultaneously the complex capacitance measurements under multiple excitation frequencies to reconstruct both permittivity and conductivity distributions of the MUT. The inherent spatial correlation of multi-frequency images is explored to improve image quality and robustness. A linearized MMV based CVMF-ECT model is derived and Alternating Direction Method of Multipliers (ADMM) [22] is utilized to solve the corresponding image reconstruction problem. We compare and demonstrate the superiority of the proposed approach over commonly used methods through real-world experiments.

This paper is organized as follows. The complex-valued ECT model are briefly reviewed in Section II. In Section III, the MMV based CVMF-ECT model is presented and the proposed image reconstruction framework is illustrated. In Section IV, an impedance analyzer based CVMF-ECT system is reported, and the performance of the proposed framework is verified and benchmarked by phantom experiments. Conclusions and future work are given in Section V.

## II. COMPLEX-VALUED ELECTRICAL CAPACITANCE TOMOGRAPHY

Conventional ECT model describes the relations between capacitance  $C$  and permittivity distribution  $\varepsilon(x, y)$  using the following integral equation [23]:

$$C = \frac{Q}{V} = -\frac{1}{V} \iint_{\Gamma} \varepsilon(x, y) \nabla \phi(x, y) d\Gamma \quad (1)$$

where  $Q$  and  $V$  denote respectively the total charge and potential difference between electrodes constituting the capacitance;  $\Gamma$  is the surface of the electrode, and  $\phi(x, y)$  represents the electric potential distribution.

By introducing a perturbation of permittivity, i.e.  $\Delta\varepsilon$ , a linear approximation of Eq. (1) can be obtained:

$$\Delta C = J \Delta\varepsilon \quad (2)$$

where  $\Delta C \in \mathbb{R}^m$  is the change of capacitance due to perturbation  $\Delta\varepsilon \in \mathbb{R}^n$ , and  $J \in \mathbb{R}^{m \times n}$  is the Jacobian matrix. Eq. (2) or its normalized format, which is also referred to as time-difference imaging model, is the most commonly adopted model in solving the ECT image reconstruction problem, which can be generally formulated as the following optimization problem:

$$\widehat{\Delta\varepsilon} = \arg \min_{\Delta\varepsilon} \{ \|\Delta C - J \Delta\varepsilon\|^2 + \mu f(\Delta\varepsilon) \} \quad (3)$$

where  $\widehat{\Delta\varepsilon} \in \mathbb{R}^n$  is the estimate of permittivity variation;  $f(\cdot)$  and  $\mu \in \mathbb{R}$  denote the regularization function and parameter, respectively.

The conventional ECT model only considers the effect of permittivity. In order to comprehensively evaluate the influence of conductive components on measurement, the recently proposed complex-valued ECT model [18] further takes the impact of conductivity variation into account by introducing complex capacitance measurements. Then Eq. (1) becomes

$$C' = -\frac{1}{V} \iint_{\Gamma} \left( \varepsilon(x, y) + \frac{\sigma(x, y)}{j\omega} \right) \nabla \phi(x, y) d\Gamma \quad (4)$$

where  $C'$  denotes the complex-valued capacitance,  $\sigma(x, y)$  is conductivity distribution, and  $\omega$  is the angular frequency of the excitation signal.

Similarly, the linearization approximation of Eq. (4) can be obtained:

$$\begin{bmatrix} \Delta C_r \\ \Delta C_i \end{bmatrix} = \begin{bmatrix} J_{r,\varepsilon} & J_{r,\sigma} \\ J_{i,\varepsilon} & J_{i,\sigma} \end{bmatrix} \begin{bmatrix} \Delta\varepsilon_r \\ \Delta\varepsilon_i \end{bmatrix} \quad (5)$$

where  $\Delta C_r, \Delta C_i \in \mathbb{R}^m$  represent respectively the real and imaginary part of the complex capacitance change;  $J_{r,\varepsilon}, J_{r,\sigma} \in \mathbb{R}^{m \times n}$  are the Jacobian matrices mapping the change of permittivity and conductivity to the real part of capacitance change; likewise,  $J_{i,\varepsilon}, J_{i,\sigma} \in \mathbb{R}^{m \times n}$  are the Jacobian matrices mapping the change of permittivity and conductivity to the imaginary part of capacitance change;  $\Delta\varepsilon_r, \Delta\varepsilon_i \in \mathbb{R}^n$  denote respectively the real and imaginary part of complex permittivity change, where  $\Delta\varepsilon_r$  is the permittivity change and

$$\Delta\varepsilon_i = -\frac{\Delta\sigma}{\omega} \quad (6)$$

where  $\Delta\sigma \in \mathbb{R}^n$  is the conductivity change.

For simplicity, Eq. (5) can be further written as

$$Z = SG \quad (7)$$

where  $Z = \begin{bmatrix} \Delta C_r \\ \Delta C_i \end{bmatrix} \in \mathbb{R}^{2m}$ ,  $S = \begin{bmatrix} J_{r,\varepsilon} & J_{r,\sigma} \\ J_{i,\varepsilon} & J_{i,\sigma} \end{bmatrix} \in \mathbb{R}^{2m \times 2n}$ , and  $G = \begin{bmatrix} \Delta\varepsilon_r \\ \Delta\varepsilon_i \end{bmatrix} \in \mathbb{R}^{2n}$ .

Solving the image reconstruction problem of complex-valued ECT then becomes the estimation of both conductivity and permittivity change, given the complex capacitance measurement and Jacobian matrix. In theory, the image reconstruction algorithms for the conventional ECT model are also applicable.

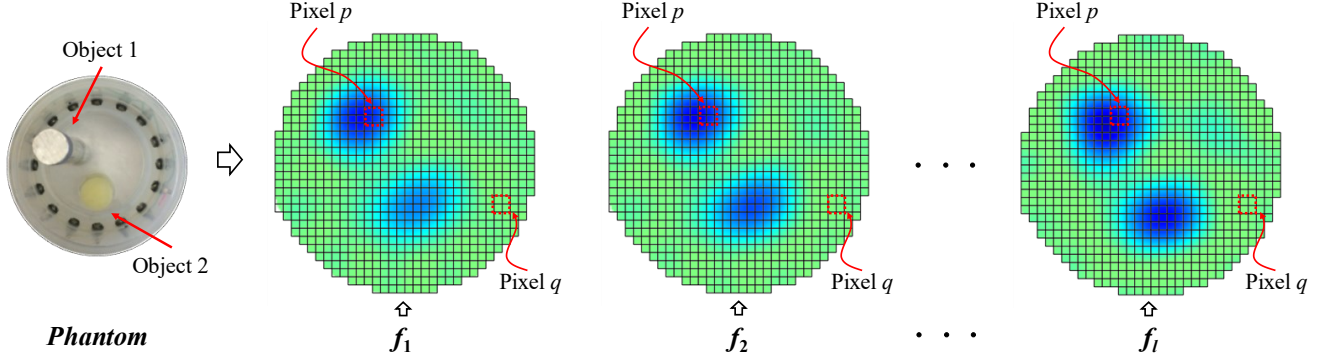


Fig. 1. Schematic illustration of pixel correlation of reconstructed images under different excitation frequencies.

### III. MMV BASED CVMF-ECT

In this Section, we first consider the simultaneous image reconstruction problem of CVMF-ECT by using MMV model. A general MMV model can be given by the following systems of equations.

$$B = AX \quad (8)$$

where  $B \in \mathbb{R}^{m \times l}$  denotes the collection of  $l$  measurement vectors,  $A \in \mathbb{R}^{m \times n}$  is the system matrix, and  $X \in \mathbb{R}^{n \times l}$  represents the collection of  $l$  unknown parameter vectors to be solved. The SMV problem is a special case of (8) where  $l=1$ .

Further, based on Eq. (7), by incorporating the complex capacitance measurement vectors under  $l$  excitation frequencies, and taking into account the fact that the Jacobian matrices under  $l$  frequencies are different, the modified MMV model of CVMF-ECT can be formulated as

$$\begin{bmatrix} Z_1 \\ Z_2 \\ \vdots \\ Z_l \end{bmatrix} = \begin{bmatrix} S_1 & & & \\ & S_2 & & \\ & & \ddots & \\ & & & S_l \end{bmatrix} \begin{bmatrix} G_1 \\ G_2 \\ \vdots \\ G_l \end{bmatrix} \quad (9)$$

where we define

- $\tilde{Z} = [Z_1 \ Z_2 \ \dots \ Z_l]^T \in \mathbb{R}^{2ml}$  is a collection of complex capacitance measurements under  $l$  different excitation frequencies;
- $\tilde{G} = [G_1 \ G_2 \ \dots \ G_l]^T \in \mathbb{R}^{2nl}$  is a collection of solutions, i.e. complex permittivity, of  $l$  frequencies; and
- $\tilde{S} = \text{diag}([S_1 \ S_2 \ \dots \ S_l]^T) \in \mathbb{R}^{2ml \times 2nl}$  denotes a collection of Jacobian matrices of  $l$  frequencies.

The simultaneous multi-frequency image reconstruction problem of CVMF-ECT is to estimate a series of complex permittivity  $\tilde{G}$  with the given measurement collection  $\tilde{Z}$  and Jacobian collection  $\tilde{S}$ .

In our formerly reported work [18], the problem was decomposed to  $l$  sub-problems by frequency, treated using SMV model and solved successively using Tikhonov Regularization (TR) [24], i.e.

$$\hat{G}_i = (S_i^T S_i + \alpha I)^{-1} S_i^T Z_i \quad (10)$$

where  $\hat{G}_i$  is the  $i^{\text{th}}$  solution;  $\alpha \in \mathbb{R}$  is the regularization parameter;  $I \in \mathbb{R}^{n \times n}$  is the identity matrix, and  $i = 1, 2, \dots, l$  denotes the index of excitation frequency. Although TR is easy to implement, it suffers from low spatial resolution and the computational cost is considerable due to matrix inversion, especially when the dimension of the Jacobian matrix is large.

In order to simultaneously reconstruct the multi-frequency images in an effective and efficient way, we consider to take advantage of the inherent correlations of individual image pixels under different frequencies. The idea is illustrated in Fig. 1. Assume a two-object phantom (see the left of Fig. 1) is imaged under different excitation frequencies, i.e.  $f_1, f_2, \dots, f_l$ , it is intuitive that the pixels of all the  $l$  images with the same indices, e.g.  $p$  and  $q$ , will demonstrate strong correlation in magnitude. Briefly, all  $G_i$  in  $\tilde{G}$  have the same/similar distribution of conductivity/permittivity variation. This structural correlation can be utilized as *a priori* information for image reconstruction.

Previous study has shown that such kind of *a priori* information can be encoded by minimizing a  $l_{2,1}$  norm of  $\tilde{G}$  [25]. Accordingly, we can formulate the simultaneous multi-frequency image reconstruction problem as

$$\begin{aligned} \min_{\tilde{G}} \quad & \|\tilde{G}\|_{w,2,1} := \sum_{i=1}^{2n} w_i \|\tilde{G}_{b_i}\|_2 \\ \text{s.t.} \quad & \tilde{S}\tilde{G} = \tilde{Z} \end{aligned} \quad (11)$$

where, we divide the elements/pixels of  $\tilde{G}$  into  $2n$  groups, i.e.  $\{\tilde{G}_{b_1}, \tilde{G}_{b_2}, \dots, \tilde{G}_{b_{2n}}\}$ , and each pixel group  $\tilde{G}_{b_i} \in \mathbb{R}^l$  denotes the  $i^{\text{th}}$  row of  $G' = [G_1 \ G_2 \ \dots \ G_l] \in \mathbb{R}^{2n \times l}$ ; in this way, the pixels of all the  $l$  images with the same indices will be grouped together. Fig. 2 further illustrates the pixel grouping method.  $w_i \in \mathbb{R}$ ,  $i = 1, \dots, 2n$ , is the weighting factor for the  $l_2$  norm of each group, which is a positive scalar. The minimization of  $\|\tilde{G}\|_{w,2,1}$  in practical will promote the row-wise sparsity of  $G'$ , whose characteristic is resulted from the inter-image correlation.

The Lagrange dual function is leveraged to solve Eq. (11), which is expressed as

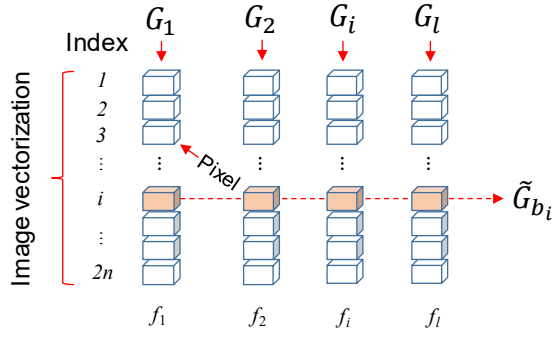


Fig. 2. Illustration of pixel grouping of multi-frequency images.

$$\max_K \left\{ \min_{\tilde{G}} \sum_{i=1}^{2n} w_i \|\tilde{G}_{b_i}\|_2 - K^T (\tilde{S}\tilde{G} - \tilde{Z}) \right\} \quad (12)$$

where  $K \in \mathbb{R}^{2nl}$  denotes an auxiliary vector. Eq. (12) is equivalent to

$$\min_K \left\{ -\tilde{Z}^T K : \|\tilde{S}_{b_i} K\|_2 \leq w_i, i = 1, 2, \dots, 2n \right\} \quad (13)$$

where  $\tilde{S}_{b_i}$  denotes the submatrix of  $\tilde{S}$ , which is a collection of columns of  $\tilde{S}$  that corresponds to the  $i^{\text{th}}$  group.

We then introduce the Alternating Direction Method of Multipliers (ADMM) to solve the optimization problem in Eq. (13) [26, 27]. Here, by introducing another auxiliary vector  $\varphi \in \mathbb{R}^{2nl}$ , Eq. (13) can be reformulated as

$$\begin{aligned} \min_{K, \varphi} & -\tilde{Z}^T K \\ \text{s. t.} & \varphi = \tilde{S}^T K, \|\varphi_{b_i}\|_2 \leq w_i, i = 1, 2, \dots, 2n \end{aligned} \quad (14)$$

The augmented Lagrangian problem of (14) is then given by

$$\begin{aligned} \min_{K, \varphi} & -\tilde{Z}^T K - \tilde{G}^T (\varphi - \tilde{S}^T K) + \frac{\lambda}{2} \|\varphi - \tilde{S}^T K\|_2^2 \\ \text{s. t.} & \|\varphi_{b_i}\|_2 \leq w_i, i = 1, 2, \dots, 2n \end{aligned} \quad (15)$$

where  $\lambda$  as a positive scalar denotes the penalty parameter.  $\tilde{G} \in \mathbb{R}^{2nl}$  is the multiplier and essentially the primal variable. Eq. (15) can be easily separated into two sub-problems and solved by applying alternating minimization. In this way, we can first obtain the  $K$  sub-problem, which is given by

$$\min_K -\tilde{Z}^T K + (\tilde{S}\tilde{G})^T K + \frac{\lambda}{2} \|\varphi - \tilde{S}^T K\|_2^2 \quad (16)$$

Eq. (16) as a convex quadratic problem can be solved iteratively via gradient descent method [28]. The iteration form is given by

$$K = K - \delta (\lambda \tilde{S}\tilde{S}^T K - \tilde{Z} + \tilde{S}\tilde{G} - \lambda \tilde{S}\varphi) \quad (17)$$

---

**Algorithm 1: MMV CVMF-ECT**


---

- 1: **Input:**  $\tilde{Z}, \tilde{S}, \beta, \lambda, k$ .
- 2: **Initialize:**  $\tilde{G} = \mathbf{0} \in \mathbb{R}^{2nl}, \varphi = \mathbf{0} \in \mathbb{R}^{2nl}$
- 3: **while**  $l \leq k$  and  $\|\zeta(\cdot)\|_2 \geq \|\tilde{G}(\cdot)\|_2$  **do**
- 4:   (1): Solve the  $K$  sub-problem using (16).
- 5:   (2): Solve the  $\varphi$  sub-problem using (18).
- 6:   (3): Update the multiplier using (19).
- 7:   (4):  $l \leftarrow l + 1$ .
- 8: **end while**

9: **Return:** the best solution of  $\tilde{G}$ .

---

where  $\delta$  is a positive scalar denoting the step length.

Likewise, the  $\varphi$  sub-problem can be formulated as

$$\begin{aligned} \min_{\varphi} & -\tilde{G}^T \varphi + \frac{\lambda}{2} \|\varphi - \tilde{S}^T K\|_2^2 \\ \text{s. t.} & \|\varphi_{b_i}\|_2 \leq w_i, i = 1, 2, \dots, 2n \end{aligned} \quad (18)$$

Easily, the solution of (18) can be obtained:

$$\varphi_{b_i} = P_{\mathcal{H}_2^i} \left\{ \tilde{S}_{b_i}^T K + \frac{1}{\lambda} \tilde{G}_{b_i} \right\}, i = 1, 2, \dots, 2n \quad (19)$$

where  $P$  denotes a projection onto a convex set, which is denoted as a subscript,  $\mathcal{H}_2^i \triangleq \{\varphi \in \mathbb{R}^{2l_i} : \|\varphi\|_2 \leq w_i\}$ . For simplicity, Eq. (19) can be equivalently formulated as

$$\varphi = P_{\mathcal{H}} \left\{ \tilde{S}^T K + \frac{1}{\lambda} \tilde{G} \right\} \quad (20)$$

where  $P_{\mathcal{H}} \triangleq \{\varphi \in \mathbb{R}^{2nl} : \|\varphi_{b_i}\|_2 \leq w_i, i = 1, 2, \dots, 2n\}$ .

Finally, the multiplier or the primal variable is updated by

$$\tilde{G} = \tilde{G} - \beta \lambda (\varphi - \tilde{S}^T K) \quad (21)$$

where  $\beta$  denotes the step length. We let  $\zeta = \beta \lambda (\varphi - \tilde{S}^T K)$  for later use.

The implementation scheme of the proposed MMV based CVMF-ECT (MMV CVMF-ECT) algorithm is summarized in *Algorithm 1*.

#### IV. RESULTS AND DISCUSSION

In this Section, we validate the feasibility of CVMF-ECT and the performance of MMV CVMF-ECT framework by real-world experiments. Comparison with the conventional ECT image reconstruction algorithms is also presented.

##### A. Sensor and phantoms

An 8-electrode ECT sensor with 60 mm external and 56 mm internal diameters was utilised in the experiments (see Fig. 3).

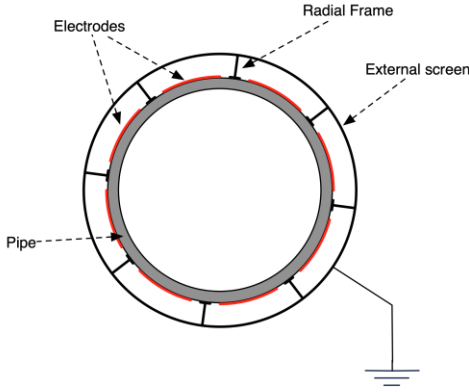


Fig. 3. Structure of the sensor.

Two different phantoms with conductive backgrounds and non-conductive anomaly were constructed (see Fig. 4). *Phantom 1* (see Fig. 4(a)) has a homogeneous saline background and a circular acrylic bar which diameter is 15mm. *Phantom 2* (see Fig. 4(b)) has the same background but three circular acrylic bars. Two different conductivity values of the background saline were tested, i.e. 0.1 S/m and 0.5 S/m, in order to demonstrate the impact of conductivity on image quality.

### B. CVMF-ECT system and experimental setup

An 8-electrode CVMF-ECT system (see Fig. 5) was established to validate the practical feasibility of CVMF-ECT. The system was constructed based on a Keysight E4990A Impedance Analyzer.

In the measurement process, we selected a series of excitation frequencies ranging from 0.1 MHz to 7 MHz with a step of 0.1 MHz. The complex capacitance measurements of each frequency were acquired and conventional ECT sensing strategy [23] was adopted, where a completed scan comprises 28 non-redundant complex capacitance measurements.

### C. Algorithm parameters

When implementing *Algorithm 1*, the maximum iteration number  $k$  is set to be 300, and we set  $\lambda = \text{mean}(\text{abs}(\tilde{Z}))$ , where  $\tilde{Z}$  is a collection of complex capacitance measurements under five excitation frequencies.  $\beta$  is fixed at 0.16 based on a fine tuning procedure by trials.

We compare *Algorithm 1* with the prevailing TR and Landweber iteration [23] in ECT. In implementation of TR (see Eq. (10)), the regularization parameter  $\alpha$  is fixed at  $1e-10$  for all frequencies based on a fine tuning procedure. The number of iterations of Landweber is selected as 3000, and the relaxation factor is 1 for both phantoms, based on trial and error.

### D. Image quality assessment

The Structural Similarity Index Measure (SSIM) is employed to quantitatively evaluate the reconstruction image quality. SSIM is commonly used in the area of image processing to evaluate the similarity between the reconstructed image and the ground truth, which is defined as [29]

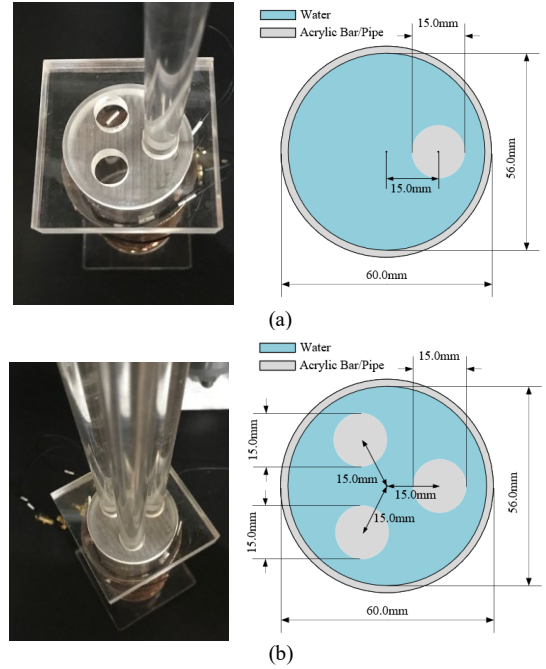


Fig. 4. Experimental phantoms. (a) Phantom 1. (b) Phantom 2.

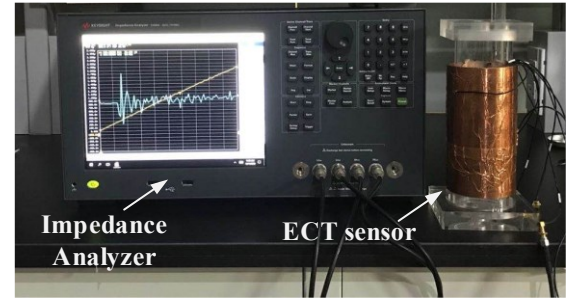
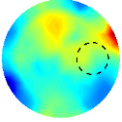
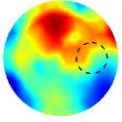
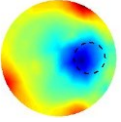
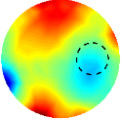
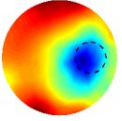
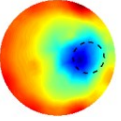


Fig. 5. The CVMF-ECT system.

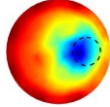
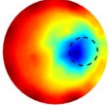
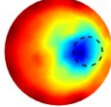
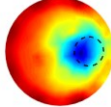
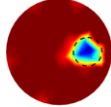
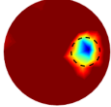
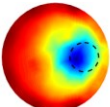
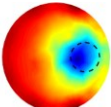
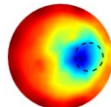
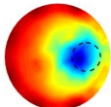
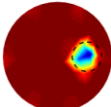
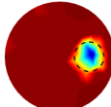
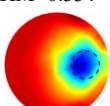
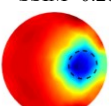
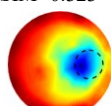
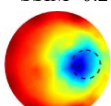
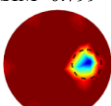
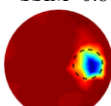
$$SSIM = \frac{(2\mu_x\mu_y + R_1)(2\sigma_{xy} + R_2)}{(\mu_x^2 + \mu_y^2 + R_1)(\sigma_x^2 + \sigma_y^2 + R_2)} \quad (22)$$

where  $x, y$  is the reconstruction results and the true distribution

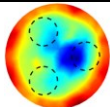
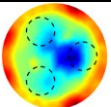
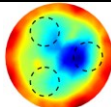
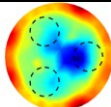
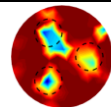
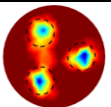
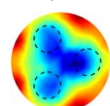
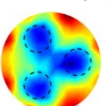
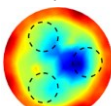
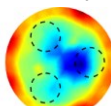
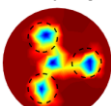
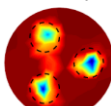
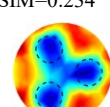
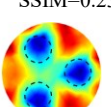
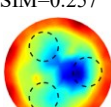
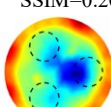
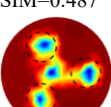
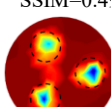
TABLE I  
COMPARISON OF CONVENTIONAL ECT AND CV-ECT OF PHANTOM 1 WITH 0.5 S·M-1 BACKGROUND CONDUCTIVITY UNDER 1.0 AND 6.5 MHz EXCITATION FREQUENCY

Frequency (MHz)	Conventional ECT		Complex-Valued ECT			
	$(\Delta\epsilon)$	$(\Delta\epsilon)$	$(\Delta\epsilon)$	$(\Delta\sigma)$		
1.0		SSIM= 0.126		SSIM= 0.099		SSIM= 0.194
6.5		SSIM= 0.187		SSIM= 0.252		SSIM= 0.242

**TABLE II**  
SIMULATION RESULTS OF PHANTOM 1 (0.5 S·M<sup>-1</sup>)

Frequency (MHz)	Tikhonov Regularization		Landweber iteration		MMV CVMF-ECT	
	Real part ( $\Delta\epsilon$ )	Imaginary part ( $\Delta\sigma$ )	Real part ( $\Delta\epsilon$ )	Imaginary part ( $\Delta\sigma$ )	Real part ( $\Delta\epsilon$ )	Imaginary part ( $\Delta\sigma$ )
0.5						
	SSIM=0.319	SSIM=0.274	SSIM=0.319	SSIM=0.274	SSIM=0.788	SSIM=0.823
3.5						
	SSIM=0.334	SSIM=0.285	SSIM=0.323	SSIM=0.273	SSIM=0.799	SSIM=0.813
6.5						
	SSIM=0.380	SSIM=0.383	SSIM=0.323	SSIM=0.271	SSIM=0.793	SSIM=0.799

**TABLE III**  
SIMULATION RESULTS OF PHANTOM 2 (0.5 S·M<sup>-1</sup>)

Frequency (MHz)	Tikhonov Regularization		Landweber iteration		MMV CVMF-ECT	
	Real part ( $\Delta\epsilon$ )	Imaginary part ( $\Delta\sigma$ )	Real part ( $\Delta\epsilon$ )	Imaginary part ( $\Delta\sigma$ )	Real part ( $\Delta\epsilon$ )	Imaginary part ( $\Delta\sigma$ )
0.5						
	SSIM=0.241	SSIM=0.204	SSIM=0.241	SSIM=0.205	SSIM=0.413	SSIM=0.489
3.5						
	SSIM=0.234	SSIM=0.239	SSIM=0.257	SSIM=0.205	SSIM=0.487	SSIM=0.493
6.5						
	SSIM=0.272	SSIM=0.277	SSIM=0.257	SSIM=0.205	SSIM=0.490	SSIM=0.492

**TABLE IV**  
EXPERIMENTAL RESULTS OF PHANTOM 1 (0.1 S/M)

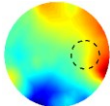
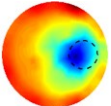
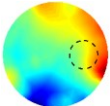
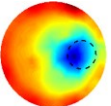
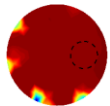
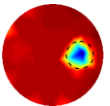
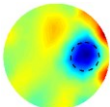
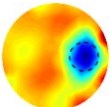
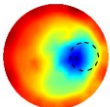
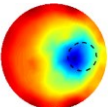
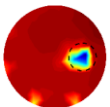
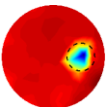
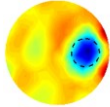
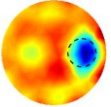
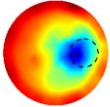
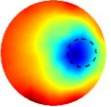
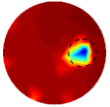
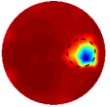
Frequency (MHz)	Tikhonov Regularization		Landweber iteration		MMV CVMF-ECT	
	Real part ( $\Delta\epsilon$ )	Imaginary part ( $\Delta\sigma$ )	Real part ( $\Delta\epsilon$ )	Imaginary part ( $\Delta\sigma$ )	Real part ( $\Delta\epsilon$ )	Imaginary part ( $\Delta\sigma$ )
0.5						
3.5						
6.5						

TABLE V  
EXPERIMENTAL RESULTS OF PHANTOM 2 (0.1 S/M)

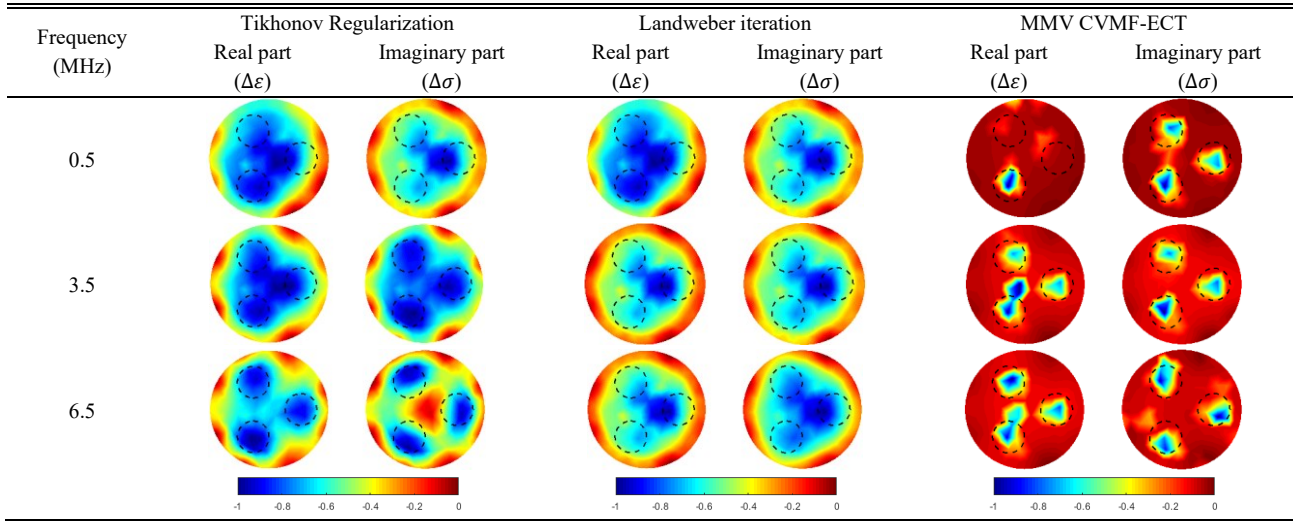


TABLE VI  
EXPERIMENTAL RESULTS OF PHANTOM 1 (0.5 S/M)

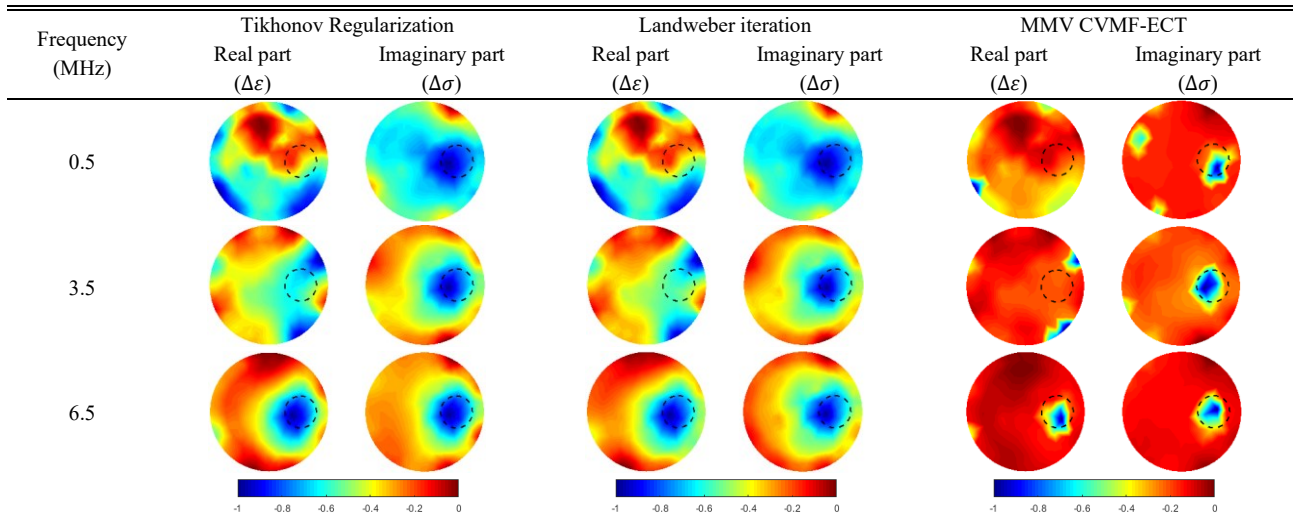
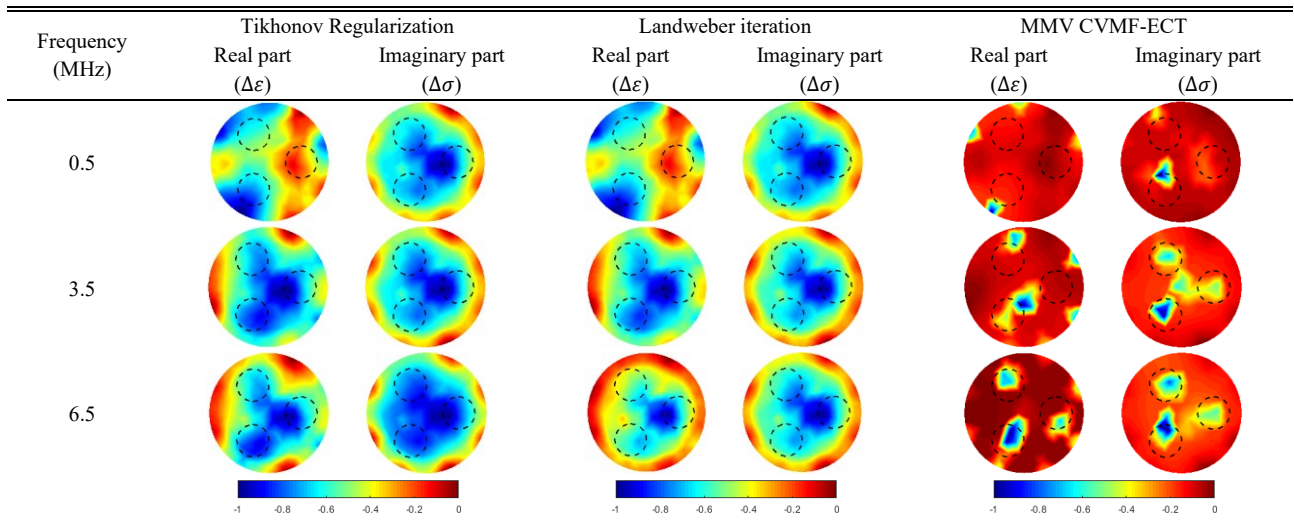


TABLE VII  
EXPERIMENTAL RESULTS OF PHANTOM 2 (0.5 S/M)





under current frequency, respectively;  $\mu_x, \mu_y, \sigma_x, \sigma_y$ , and  $\sigma_{xy}$  denote respectively the local means, standard deviations, and cross-covariance for images  $x, y$ ;  $R_1, R_2$  are the regularization constants for the luminance and contrast.

### E. Comparison with conventional ECT

TABLE I compares the reconstruction images of conventional ECT and CVMF-ECT for *Phantom 1* based on Landweber iteration. The background conductivity is 0.5 S/m and two excitation frequencies, i.e. 1 MHz and 6.5 MHz, are employed.

In conventional ECT, the measurement is the amplitude of the complex capacitance, i.e.  $abs(C_r + C_i)$ , and the reconstruction is permittivity change only. Observing the results, conventional ECT can hardly reconstruct the acrylic bar in the saline for both two excitation frequencies. In comparison, at the frequency of 1 MHz, the permittivity reconstruction of CVMF-ECT fails as well, but the conductivity image succeeds to distinguish the bar from the background. Increasing the frequency to 6.5 MHz, both permittivity and conductivity images of CVMF-ECT show the object clearly. The results demonstrate that CVMF-ECT solves the complex capacitance nature of the measurement better than conventional ECT.

### F. Numerical results

To assess the feasibility of the CVMF-ECT, simulation of *Phantom 1* and *Phantom 2* (see Fig. 4) with 0.5 S/m background conductivity is conducted using Finite Element Analysis (FEA). The images are reconstructed by using TR, Landweber and MMV CVMF-ECT respectively and are shown in TABLE II and TABLE III. Meanwhile, the SSIM of each image is listed. For both phantoms and three frequencies, i.e. 0.5 MHz, 3.5 MHz and 6.5 MHz, the results of MMV CVMF-ECT clearly outperform the others. It preliminarily verifies the validity of CVMF-ECT and the effectiveness of the proposed MMV based method.

### G. Experimental results

When there are highly conductive contents in conventional ECT sensor area, the image reconstruction results are inaccurate because of the inaccurate sensitivity map [30].

TABLE IV and TABLE V present the multi-frequency image reconstruction results of *Phantom 1* (see Fig. 4(a)) and *Phantom 2* (see Fig. 4(b)) by using TR, Landweber and MMV CVMF-ECT, respectively. In the two experiments, the background conductivity is 0.1 S/m. The TR results and Landweber iteration results at three frequencies, i.e. 0.5 MHz, 3.5 MHz and 6.5 MHz, were reconstructed subsequently whilst the MMV CVMF-ECT results were reconstructed simultaneously. The black dashed lines in the reconstructed images denote the true location and size of the objects. We can see that for *Phantom 1*, both real part, which stands for the permittivity change  $\Delta\epsilon$ , and the imaginary part, which stands for the conductivity change  $\Delta\sigma$ , can be reconstructed by TR, Landweber and MMV CVMF-ECT. However, TR and Landweber results suffer from severe distortion and artifacts at all the given frequencies. Regarding *Phantom 2*, it is difficult to identify how many objects exist within the ROI owing to the distinct artifacts for both TR and

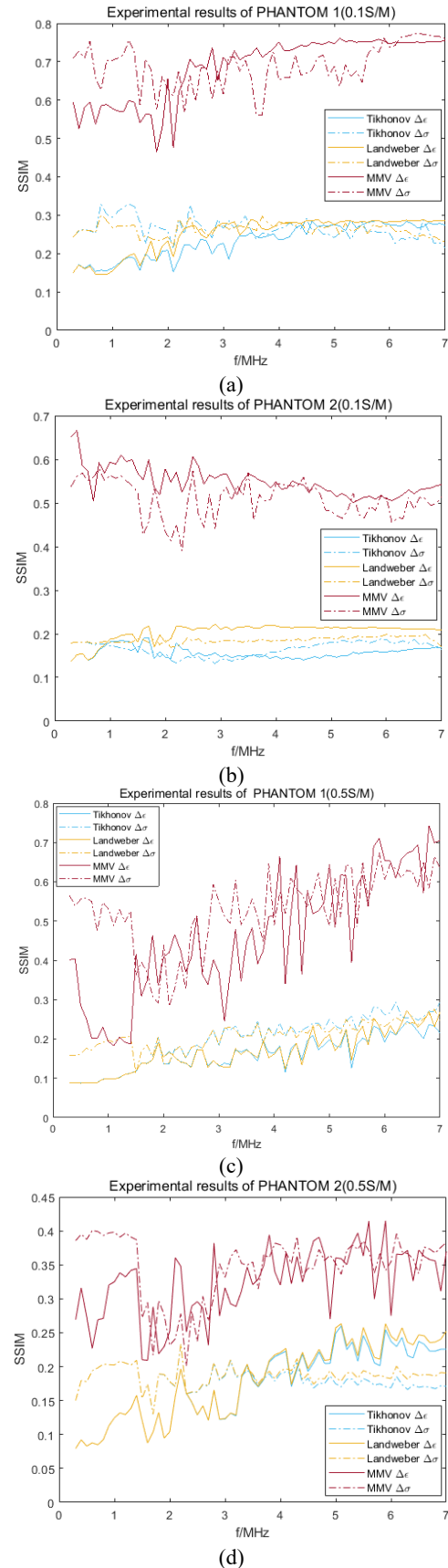


Fig. 6. SSIM of (a) results of *Phantom 1* (0.1 S/M), (b) results of *Phantom 2* (0.1 S/M), (c) results of *Phantom 1* (0.5 S/M), and (d) results of *Phantom 2* (0.5 S/M).

Landweber results. In contrast, for both phantoms, the MMV CVMF-ECT results significantly outperform the other results in terms of noise reduction, shape and location accuracy.

We also evaluated the imaging performance of the three algorithms under a higher background conductivity. Another two experiments which adopted the same phantom setups with Fig. 4 but with a higher background conductivity of 0.5 S/m were carried out. TABLE VI and TABLE VII show the multi-frequency image reconstruction results of the two phantoms at three given frequencies, i.e. 0.5 MHz, 3.5 MHz and 6.5 MHz, respectively. In our formerly reported work [18], it has been confirmed that the increase of background conductivity brings in challenge in reconstructing the permittivity part. Since the complex valued capacitance measurement,  $C'$  in Eq. (4) is based on both permittivity and conductivity distribution, the conductivity has a stronger impact on the measurement when the frequency isn't high enough, i.e.  $\frac{\sigma(x,y)}{\omega} \gg \varepsilon(x,y)$ . Therefore in the saline of 0.5 S/m, it is difficult to distinguish the change in the permittivity distribution. Overall, the multi-frequency image reconstruction results of the two phantoms show consistency with the simulation analysis in [18]. That is, the real part, i.e. the permittivity change  $\Delta\varepsilon$ , can hardly be reconstructed, but the imaginary part, i.e. the conductivity change  $\Delta\sigma$ , can be stably recovered for all the testing frequencies. In regard to the reconstruction of imaginary part of *Phantom 1* (see TABLE VI), TR and Landweber results can roughly demonstrate the location and shape of the object but there are still apparent distortions and the background artifacts are non-negligible. Differently, MMV CVMF-ECT results clearly give more accurate estimation of object shape and location, meanwhile with significantly reduced artifacts.

As for results of *Phantom 2* (see TABLE VII), the three objects can barely be identified in the imaginary parts of TR and Landweber results, due to the blurred boundaries and the existence of very strong background artifacts. However, the MMV CVMF-ECT results show similar performance with the lower background conductivity setup. Both the location and shape of the three objects can be explicitly recovered. This further verifies the image quality and robustness of CVMF-ECT can be greatly enhanced with MMV model.

As shown in Fig. 6, the SSIM of MMV CVMF-ECT results are much higher than TR and Landweber. The quality of reconstructed images from the experimental data tends to be improved when the excitation frequency increases for highly conductive background ( $\sigma = 0.5$  S/m). This suggests that both the real part and the imaginary part can be better reconstructed under higher excitation frequencies when background conductivity is high.

The MMV approach also stands out for its high computational efficiency. All the algorithms were implemented in MABLAB R2018b, on a computer with Intel i5-9400F CPU@2.9GHz and 16.0 GB RAM Memory. The elapsed time for reconstructing multi-frequency images is shown in TABLE VIII. For the experiments with the background conductivity of 0.1 S/m and 0.5 S/m, the mean elapsed time of MMV CVMF-ECT and Landweber for reconstructing *Phantom 1* and

TABLE VIII  
ELAPSED TIME FOR MULTI-FREQUENCY IMAGE RECONSTRUCTION

Algorithms	TR	Landweber	MMV
Time(s)	0.134	3.046	0.142

*Phantom 2* is 0.142s and 3.046s respectively. The consumed time of MMV is close to TR (0.134s), which is a one-step inverse solver. This indicates the potential to implement the proposed approach in real-time applications.

## V. CONCLUSION

This paper presents a novel image reconstruction framework for Complex-Valued, Multi-Frequency Electrical Capacitance Tomography (CVMF-ECT), and a practical imaging system for experimental validation of this new concept. Multiple Measurement Vector (MMV) model was introduced to simultaneously reconstruct the permittivity and conductivity distributions under the multi-frequency configuration. The proposed method uniquely utilizes the correlation of multi-frequency images to enhance image quality and meanwhile preserve low computational cost. The feasibility of the MMV CVMF-ECT framework was validated for the first time by using experimental data. Compared with conventional image reconstruction methods, significant improvements have been achieved in terms of image quality and robustness to noise. The outcomes of this work could facilitate the wide application of CVMF-ECT in practical scenarios.

In the future, we will develop a customized CVMF-ECT system by extending the conventional ECT hardware design.

## REFERENCES

- [1] Y. J. Yang and L. H. Peng, "Data Pattern With ECT Sensor and Its Impact on Image Reconstruction," (in English), *Ieee Sensors Journal*, vol. 13, no. 5, pp. 1582-1593, May 2013.
- [2] C. G. Xie *et al.*, "Electrical capacitance tomography for flow imaging: system model for development of image reconstruction algorithms and design of primary sensors," *Iee Proceedings-G Circuits Devices and Systems*, vol. 139, no. 1, pp. 89-98, Feb 1992.
- [3] X. Deng and W. Yang, "Fusion research of electrical tomography with other sensors for two-phase flow measurement," *Measurement Science Review*, vol. 12, no. 2, pp. 62-67, 2012.
- [4] Z. Huang, B. Wang, and H. Li, "Application of electrical capacitance tomography to the void fraction measurement of two-phase flow," *Instrumentation and Measurement, IEEE Transactions on*, vol. 52, no. 1, pp. 7-12, 2003.
- [5] Y. Li *et al.*, "Gas/oil/water flow measurement by electrical capacitance tomography," *Measurement Science & Technology*, vol. 24, no. 7, Jul 2013, Art. no. Unsp 074001.
- [6] Y. J. Yang, L. H. Peng, and J. B. Jia, "A novel multi-electrode sensing strategy for electrical capacitance tomography with ultra-low dynamic range," (in English), *Flow Measurement and Instrumentation*, vol. 53, pp. 67-79, Mar 2017.
- [7] Y. Liu, Y. Deng, M. Zhang, P. Yu, and Y. Li, "Experimental measurement of oil-water two-phase flow by data fusion of electrical tomography sensors and venturi tube," *Measurement Science and Technology*, vol. 28, no. 9, p. 095301, 2017.
- [8] E. A. Hammer and G. Fosssdal, "A new water-in-oil monitor based on high frequency magnetic field excitation," *2nd International Symposium Process Tomography*, 2002, pp. 9-16.
- [9] E. A. Hammer, F. Pettersen, and A. Nødseth, "Numerical simulation of eddy current losses in high frequency magnetic field water fraction meters," *3rd World Congress on Industrial Process Tomography*, 2003.
- [10] E. Hammer, E. Abro, E. Cimpan, and G. Yan, "High-frequency magnetic field probe for determination of interface levels in separation tanks," in

- Process Imaging for Automatic Control*, 2001, vol. 4188, pp. 294-299: International Society for Optics and Photonics.
- [11] M. Zhang, L. Ma, and M. Soleimani, "Dual modality ECT-MIT multi-phase flow imaging," *Flow Measurement and Instrumentation*, vol. 46, no. 0, pp. 240-254, 2015.
- [12] B. Wang, W. Tan, Z. Huang, H. Ji, and H. Li, "Image reconstruction algorithm for capacitively coupled electrical resistance tomography," *Flow Measurement and Instrumentation*, vol. 40, no. 0, pp. 216-222, 12// 2014.
- [13] B. Wang, W. Zhang, Z. Huang, H. Ji, and H. Li, "Modeling and optimal design of sensor for capacitively coupled electrical resistance tomography system," *Flow Measurement and Instrumentation*, vol. 31, no. 0, pp. 3-9, 6// 2013.
- [14] B. Wang, Y. Hu, H. Ji, Z. Huang, and H. Li, "A Novel Electrical Resistance Tomography System Based on C4D Technique," *Instrumentation and Measurement, IEEE Transactions on*, vol. 62, no. 5, pp. 1017-1024, 2013.
- [15] C. Gunes, S. M. Chowdhury, C. E. Zuccarelli, Q. M. Marashdeh, and F. L. Teixeira, "Displacement-Current Phase Tomography for Water-Dominated Two-Phase Flow Velocimetry," *IEEE Sensors Journal*, vol. 19, no. 4, pp. 1563-1571, 2018.
- [16] C. Gunes, Q. M. Marashdeh, and F. L. Teixeira, "A comparison between electrical capacitance tomography and displacement-current phase tomography," (in English), *IEEE Sensors Journal*, vol. 17, no. 24, pp. 8037-8046, Dec 15 2017.
- [17] Y. Jiang and M. Soleimani, "Capacitively Coupled Phase-based Dielectric Spectroscopy Tomography," *Sci Rep*, vol. 8, no. 1, p. 17526, Dec 3 2018.
- [18] M. Zhang and M. Soleimani, "Simultaneous reconstruction of permittivity and conductivity using multi-frequency admittance measurement in electrical capacitance tomography," (in English), *Measurement Science and Technology*, vol. 27, no. 2, p. 025405, Feb 2016.
- [19] Y. Li and M. Soleimani, "Imaging conductive materials with high frequency electrical capacitance tomography," *Measurement*, vol. 46, no. 9, pp. 3355-3361, 11// 2013.
- [20] Y. D. Jiang and M. Soleimani, "Capacitively Coupled Electrical Impedance Tomography (CCEIT) for Brain Imaging," *IEEE Trans Med Imaging*, Jan 25 2019.
- [21] S. F. Cotter, B. D. Rao, K. Engan, and K. Kreutz-Delgado, "Sparse solutions to linear inverse problems with multiple measurement vectors," (in English), *Ieee Transactions on Signal Processing*, vol. 53, no. 7, pp. 2477-2488, Jul 2005.
- [22] E. Ghadimi, A. Teixeira, I. Shames, and M. Johansson, "Optimal Parameter Selection for the Alternating Direction Method of Multipliers (ADMM): Quadratic Problems," (in English), *Ieee Transactions on Automatic Control*, vol. 60, no. 3, pp. 644-658, Mar 2015.
- [23] W. Q. Yang and L. H. Peng, "Image reconstruction algorithms for electrical capacitance tomography," (in English), *Measurement Science and Technology*, vol. 14, no. 1, pp. R1-R13, Jan 2003.
- [24] L. H. Peng, H. Merkus, and B. Scarlett, "Using regularization methods for image reconstruction of electrical capacitance tomography," (in English), *Particle & Particle Systems Characterization*, Article vol. 17, no. 3, pp. 96-104, Oct 2000.
- [25] A. Majumdar and R. Ward, "Rank Awareness in Group-Sparse Recovery of Multi-Echo MR Images," (in English), *Sensors*, vol. 13, no. 3, pp. 3902-3921, Mar 2013.
- [26] Y. J. Yang and J. B. Jia, "An Image Reconstruction Algorithm for Electrical Impedance Tomography Using Adaptive Group Sparsity Constraint," (in English), *Ieee Transactions on Instrumentation and Measurement*, vol. 66, no. 9, pp. 2295-2305, Sep 2017.
- [27] Y. J. Yang, H. C. Wu, and J. B. Jia, "Image Reconstruction for Electrical Impedance Tomography Using Enhanced Adaptive Group Sparsity With Total Variation," (in English), *Ieee Sensors Journal*, vol. 17, no. 17, pp. 5589-5598, Sep 1 2017.
- [28] C. C. Gonzaga and R. M. Schneider, "On the steepest descent algorithm for quadratic functions," (in English), *Computational Optimization and Applications*, vol. 63, no. 2, pp. 523-542, Mar 2016.
- [29] Z. Wang, A. C. Bovik, H. R. Sheikh, and E. P. Simoncelli, "Image quality assessment: from error visibility to structural similarity," *IEEE transactions on image processing*, vol. 13, no. 4, pp. 600-612 %@ 1057-7149, 2004.
- [30] M. Zhang, L. Ma, and M. Soleimani, "Magnetic induction tomography guided electrical capacitance tomography imaging with grounded conductors," *Measurement*, vol. 53, pp. 171-181 %@ 0263-2241, 2014.